Proceedings of FEDSM2006
2006 ASME Joint U.S.-European Fluids Engineering Summer Meeting
July 17-20, 2006, Miami, FL, USA

FEDSM2006-98282

LARGE EDDY SIMULATION OF FILM COOLING FLOW ABOVE A FLAT PLATE FROM INCLINED CYLINDRICAL HOLES

Ioulia V. Iourokina
Department of Aeronautics and Astronautics
Stanford University
Stanford, California 94305
Email: iouroki@stanford.edu

Sanjiva K. Lele
Department of Aeronautics and Astronautics
Stanford University
Stanford, California 94305
Email: lele@stanford.edu

ABSTRACT

Large Eddy Simulation of a realistic film cooling configuration is performed, consisting of a large plenum feeding a periodic array of short film cooling holes with length to diameter ratio $L/d = 3.5$. Film cooling jets are issued at 35 degrees into the turbulent crossflow boundary layer above the flat surface. Time-averaged flowfield is analyzed to reveal steady and unsteady structures occurring as a result of plenum-jet-crossflow interactions. Among these structures are the flow separation inside the film-hole, reverse flow zone right behind the jet injection and the counter-rotating vortex pair in the wake of the jet. All of these structures influence the wall temperature distribution and have a negative effect on film cooling effectiveness.

INTRODUCTION

The first stage of the turbine blade experiences a harsh thermal environment. The flows exiting the combustion chamber is at high temperatures exceeding the melting point of the turbine blade material and is highly turbulent. In order to avoid the detrimental effect of contact between hot gases and blade surface, cooling measures are employed, film cooling being one of them. However, since film cooling implies taking some gas out of the compressor, a compromise must be found between the overall engine efficiency and reliability to handle the thermal stresses. Accurate numerical simulations of this problem can help in identifying beneficial approaches to film cooling design.

There have been numerous attempts to study film cooling problem both experimentally and computationally. Among important observations of the researchers was strong dependence of the film cooling flow on the geometry of the film-hole as well as the supply plenum. Simon et al. [1] studied the effect of the film hole length-to diameter ratio. Leylek et al. [2, 3] investigated the effect of shaping of film holes. Peterson and Plesniak [4] showed the influence of the direction of the flow in the supply channel. The conclusion follows is that in order to predict the film cooling flow with reasonable accuracy, one has to incorporate the exact geometry of the film-holes and the supply plenum in the simulations, and not substitute the cooling gas injection with some artificial boundary conditions.

It is possible to list several computational studies of film cooling flows, where the exact geometry of the film-holes and the plenum was incorporated [2, 3, 5]. However, all these studies used the time-averaged (so called Reynolds-averaged) Navier-Stokes equations (RANS method). RANS simulations capture only the averaged flow variables and thus use relatively coarse mesh. It is a practical and commonly used method for simulating flows over complex geometries. However, due to the limited capability of RANS turbulence models, it does not provide an accurate prediction of flows with complex turbulent structures, as film cooling flows. Large Eddy Simulation (LES) can resolve time-dependent turbulence structures directly and only requires a model for the subgrid-scale terms, which are more universal and easier to model. Numerical simulations of film cooling flows using LES have also been attempted recently [6, 7]. These studies even incorporated the film hole into the simulations. But, typically, unrealistically long delivery tubes were used and inflow parabolic profile was supplied at the beginning of the delivery tube, instead of modeling the supply plenum. As it was shown by some researchers [8, 9], the connection between the plenum and the film-hole causes the flow to separate from the downstream wall of the film-hole and create a blockage effect, which pushes majority of the film-hole flow to exit into the crossflow from the upstream portion of the hole. This effect is especially pronounced when the hole is inclined. To capture these effects it is necessary to capture the full geometry.

Large Eddy Simulations of a film cooling flow above the flat surface are presented in this paper. The simulations model the exact geometry of film cooling experiments of Pietrzyk et al. [10]. It includes large sink-type delivery plenum, periodic array of 11 short film cooling holes with length-to diameter ratio of $L/d = 3.5$ and the crossflow section. Results of the simulations are analyzed and compared with the experimental data of Pietrzyk et al. [10].

NUMERICAL METHOD

Numerical method specially developed for this problem consists of coupled simulations using multiple computational codes. A fully compressible LES code is used in the area above the flat plate, while a low Mach number LES code is employed in the plenum and film holes. The motivation for using different codes comes from the essential difference of the nature of the flow in these different regions. The flat surface, which is being cooled, models the turbine blade surface, and compressibility effects are important for the flow above the turbine blade. In the plenum, on the other hand, compressibility effects are not only unimportant, but the actual Mach number is so low, that use of the compressible code in that region would significantly slow down the computations. Low Mach number code would therefore be a logical choice for the plenum/film-hole region. The two computational codes are described below.

Compressible Code

Compressible code which is used in the region above the flat plate was developed by Z.Xiong [11]. Compressible Navier-Stokes equations in primitive variables are solved numerically using implicit time integration with an approximately-factorized difference scheme. The spatial discretization is achieved by mapping the body-fitted mesh coordinates from physical space (x, y, z) to the uniform computational space (ξ, η, ζ). Fourth-order accurate central-difference scheme is used for first - and second- derivatives in the computational space. Details of the numerical implementation of the compressible code can be found in Ref. 12.

Low Mach Number Code

Low Mach number code which is used in the plenum and film holes is due to C. Pierce [13]. The set of equations solved numerically is the low Mach number approximation of the Navier-Stokes equations written in conservative form in cylindrical coordinates. Velocity components are staggered with respect to density and other scalars in both space and time [14]. Second order central difference scheme is used for the integration of momentum equations, while QUICK scheme [15] is employed for scalar advection to avoid the formation of spatial oscillations. Second-order Crank-Nickolson scheme with sub-iterations is used for time advancement. Advection and diffusion terms in radial and azimuthal directions are treated implicitly. Poisson equation for pressure is solved with the multigrid method. For more details, the reader is referred to Ref. 13.

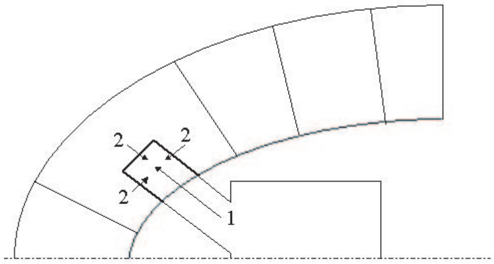

Figure 1. SAMPLE COMPUTATIONAL DOMAIN FOR THE CALCULATION OF FILM COOLING GEOMETRY.

Both codes are written in LES formulation with dynamic Smagorinsky eddy-viscosity model [16] used for the treatment of subgrid-scale terms.

Combining the Codes

The major challenge in combining compressible and low Mach number codes together is to specify an accurate and stable way of supplying the variables across the interfaces. In the present method, we use overlapping grids, where computational domain of one code has an area of overlap with the domain of another code. A sample computational domain, which includes the region above the leading edge of a turbine blade, and a film hole with a plenum, is shown in figure 1. Compressible code domain corresponds to the region exterior to the turbine blade and shown as striped in figure 1. Low Mach number code domain corresponds to a plenum and film hole in figure 1.

Only one boundary of the compressible code domain intersects the low Mach number code domain. This boundary is part of the turbine blade surface, and the intersection occurs at the place, where cooling gas is injected. Variables from the low Mach number code should be supplied to the compressible code at this location, which is schematically shown by the arrow 1 in figure 1. Boundaries of the low Mach number code domain which intersect the compressible code domain are shown in bold lines in figure 1. These are "free" boundaries of the low Mach number code domain, since they are not part of film hole walls. Variables from the compressible code should be supplied to the low Mach number code at these boundaries, which is schematically shown by arrows 2 in figure 1.

Variables Supplied From the Low Mach Number Code to the Compressible Code Variables, which are solved for in the compressible code, are $\{\rho, u, v, w, T\}$. All these variables should be specified at the location of cooling gas injection. Various ways of specifying these variables have been tested (the details of the test cases are described in [17]). However, the best performance was achieved by interpolating all of the variables $\{\rho, u, v, w, T\}$ from the low Mach number code.

Variables Supplied From the Compressible Code to the Low Mach Number Code In the low Mach number code boundary conditions are required for the following variables. Momentum equations need values of three components of velocity $\{u, v, w\}$ at the boundaries. Scalar transport equation requires specification of a scalar (temperature) at the boundary. Density is obtained from temperature through the equation of state, therefore, no boundary conditions for density is required. $\{u, v, w, T\}$ are interpolated from compressible code at the "free" boundaries of low Mach number code domain (boundary surfaces of low Mach number code domain intersecting compressible code domain). The same procedure is applied regardless of whether the "free" boundary corresponds to an inflow or outflow.

In addition, we need boundary conditions for pressure for solving the Poisson equation. In the low Mach number approximation only the second order pressure $P^{(2)}(\vec{x},t)$ enters the equations of motion (see, for example, Ref. 18). It is decoupled from density and temperature fluctuations and determined by the constraint on the divergence of velocity, much like the pressure in incompressible equations. Zeroth-order pressure $P^{(0)}(t)$ plays the role of the global thermodynamic pressure and enters the equation of state. Pressure field obtained in compressible equations is $P^{compr}(\vec{x},t) = P^{(0)}(t) + P^{(2)}(\vec{x},t)$. Taking gradient of P we have $\nabla P(\vec{x},t) = \nabla P^{(2)}(\vec{x},t)$.

In the present method, we solve the Poisson equation with Neumann boundary conditions for $P^{(2)}$. We specify the value of derivative $\frac{\partial P^{(2)}}{\partial \vec{n}}$ in the direction normal to the boundary surface. We interpolate $\frac{\partial P^{(2)}}{\partial \vec{n}} = \frac{\partial P^{compr}}{\partial \vec{n}}$ from the gradients of the compressible pressure field at the "free" boundaries of low Mach number code domain intersecting the compressible code domain. Zeroth-order pressure $P^{(0)}$ is then added to the calculated field of $P^{(2)}$ in order to set the right value of the total static pressure. We find the value of $P^{(0)}$ by matching $P^{compr} = P^{(0)} + P^{(2)}$ at one specific location in the region of overlap.

$\delta_{i,fc}/d$	$\delta^*_{i,fc}/d$	$\theta_{i,fc}/d$	$Re_{\theta i,fc}$
0.52	0.089	0.059	946

Table 1. CROSSFLOW BOUNDARY LAYER CHARACTERISTICS.

Other choices for specifying boundary conditions at the "free" boundaries of the low Mach number code domain are possible, for example, Dirichlet boundary conditions for the Poisson equation, normal derivatives for velocities instead of velocities itself. However, the method described above proved to work the best.

We use bilinear interpolation to interpolate values both from compressible to low Mach number code and from low Mach number to compressible code. Since the low Mach number code has a second-order accurate space discretization, increasing the order of interpolation beyond the second order does not lead to any further advantage.

The current method has been thoroughly tested on both steady and unsteady problems and shows good performance, which is documented in [17].

FILM COOLING SIMULATIONS

Setup of the Problem

The geometry of the problem corresponds to the film cooling experiments of Pietrzyk et al. [10]. All geometrical scales in the problem are non-dimensionalized by the diameter of the film-hole d. Large cylindrical plenum with the height $20d$ and radius $10.526d$ feeds 11 cylindrical holes with length-to diameter ratio $L/d = 3.5$. Film cooling holes are spaced uniformly in spanwise direction with the pitch $3d$. Film-holes are inclined at 35 degrees with respect to the flat surface. Experiments of [10] are incompressible, so small value of Mach number $M = 0.15$ is used here for the compressible code.

Characteristics of the crossflow boundary layer in the absence of the cooling gas injection at $x/d = -2$ are summarized in Table 1. Here $\delta_{i,fc}$, $\delta^*_{i,fc}$ and $\theta_{i,fc}$ denote 99%, displacement and momentum boundary layer thicknesses at the inflow boundary of the film cooling domain, respectively. $Re_{\theta_{i,fc}} = U_\infty \theta_{i,fc}/\nu$ is the Reynolds number based on the free-stream velocity and $\theta_{i,fc}$. These characteristics correspond to a turbulent boundary layer. To specify realistic turbulent inflow for film cooling simulations, a separate Large Eddy Simulation of turbulent boundary layer is performed to create a database, which is then fed as inflow boundary conditions into the main simulations. LES of turbulent boundary layer is accomplished with the use of rescaling-recycling technique of [19] and compressibility correction proposed by [20], slightly relaxed due to the small value of Mach number in the preset case. Details of the simulations can be found in [21].

Computational domain for the compressible code is the box with dimensions $7.5d \times 2d \times 3d$. The cooled surface is a flat plate spanning the range $x/d = (-2;5.5)$, where the point $(x/d = 0, y/d = 0)$ is located on the wall at the leading edge of the jet. Because of the elliptical shape of the hole, the trailing edge is located at $x/d = 1.74$. The grid with $128 \times 128 \times 128$ nodes is used in the simulations. Hyperbolic-tangent stretching is utilized in wall-normal direction to cluster points in the wall boundary layer. Uniform grid is used in streamwise and spanwise directions due to the occurrence of high-intensity fluctuations at any location after the cooling gas injection. The plenum and the film hole use $256 \times 128 \times 64$ and $128 \times 64 \times 64$ grid points respectively. Only one hole is simulated here, however, periodic boundary conditions in spanwise direction make it similar to the periodic array of holes. Overlap regions exist between both plenum and a film hole and between a film hole and a compressible domain. Plenum is coupled to the film hole by the same coupling procedure as described above, but applied to two low Mach number codes. $x-z$ view of the computational domain used in the simulations is shown in figure 2.

Uniform velocity profile is specified at the entrance into the plenum, giving the velocity ratio $VR = U_j/U_\infty = 0.64$, where U_j is the jet velocity and U_∞ is the crossflow free-stream velocity. Density ratio $DR = \rho_j/\rho_\infty = 0.95$ is used in the present simulations. The rest of the boundaries of the plenum and the pipe correspond to either walls with no-slip and adiabatic boundary conditions or boundaries of the overlapping region, where interface boundary conditions are set. For the compressible code domain we use no-slip adiabatic boundary conditions for the wall, interface conditions in the region of the jet injection, uniform free-stream at the top and parabolized Navier-Stokes equations at the outflow. Turbulent boundary layer profile taken from an auxiliary LES simulations is specified at the inflow.

Artificial Dissipation

Numerical method for the compressible code uses fourth-order central difference discretization for spatial terms. Because of its symmetric stencil, central-difference scheme is non-dissipative, unlike numerical schemes with biased stencils, such as upwind schemes. The lack of numerical dissipation can result in numerical instability due to the generation of unresolved high wave number components by nonlinear flow interactions. This effect is especially severe when the gradients of the flow parameters are high, as it occurs in the places of shear between the injected jet and the crossflow. In order to damp these unresolved components, a fourth-order artificial dissipation is introduced by adding the following term to the right-hand side of Navier-Stokes equations

$$D = -\sigma_d(\xi,\eta,z,t)\left(\Delta\xi^4\frac{\partial^4 U}{\partial\xi^4} + \Delta\eta^4\frac{\partial^4 U}{\partial\eta^4} + \Delta z^4\frac{\partial^4 U}{\partial z^4}\right), \quad (1)$$

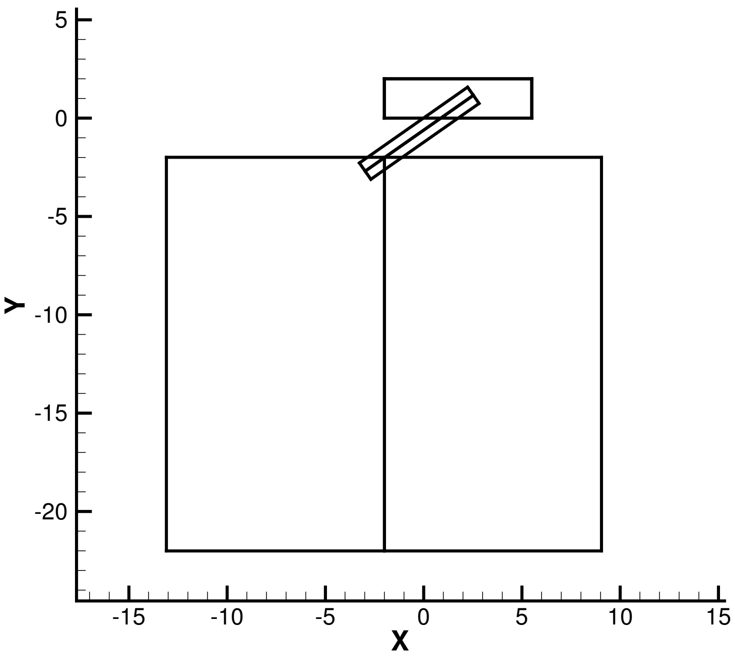

Figure 2. $X-Z$ VIEW OF THE COMPUTATIONAL DOMAIN FOR LES OF FILM COOLING.

where $U = \{\rho, u, v, w, T\}^T$ is the vector of flow variables and $\sigma_d(\xi,\eta,z,t)$ is the coefficient, which controls the amount of the added dissipation. The regions, where high wave number components are generated and artificial dissipation is required, are not fixed in space and time, but depend on the local state of the flow. To make sure that the model removes the energy above the Nyquist wavenumber without corrupting the remaining flow, a special form for the coefficient $\sigma_d(\xi,\eta,z,t)$ is proposed, proportional to the high-order derivatives of the local strain rate. It imparts spectral-like behavior to the model, thus eliminating the need for *ad hoc* limiters to reduce the value of the coefficient σ_d in smooth regions. The formulation used in the current method is based on the ideas of the hyperviscosity model proposed by Cook et al. [22, 23] and hyperdiffusivity model of Fiorina et al. [24].

In multiple dimensions, the coefficient σ_d can be written as

$$\sigma_d(\xi,\eta,z,t) = \varepsilon_d \Delta^{r+1}\overline{|\nabla^r S|}, \quad (2)$$

where ε_d is the model constant, $\Delta = (\Delta\xi\Delta\eta\,\Delta z)^{1/3}$ is the local grid spacing, $S = (S_{ij}S_{ij})^{1/2}$ is the magnitude of the rate of strain tensor and ∇^r is the polyharmonic operator which defines a sequence of Laplacians. For example, $r = 2$ corresponds to a single Laplacian $\nabla^2 S$, $r=4$ leads to the biharmonic operator $\nabla^4 S = \nabla^2(\nabla^2 S)$ and so on. The overbar $(\overline{f})$ denotes a truncated-Gaussian filter, defined as

$$\overline{f}(x) = \int_{-L}^{L} G\left(|x-x'|;L\right) f(x')\, d^3x', \tag{3}$$

where

$$G(x';L) = \frac{e^{-6x'^2/L^2}}{\int_{-L}^{L} e^{-6x'^2/L^2} d^3x'}, \quad L = 4\Delta. \tag{4}$$

This filter eliminates cusps introduced by the absolute value operator in (2), which, in turn, ensures that the value of σ_d is positive, and the added terms (1) perform stabilizing function. In the present work, (4) is approximated along each grid line as

$$\begin{aligned}\overline{f}_j = \tfrac{3565}{10,368} f_j + \tfrac{3091}{12,960}(f_{j-1}+f_{j+1}) + \tfrac{1997}{25,920}(f_{j-2}+f_{j+2}) \\ + \tfrac{149}{12,960}(f_{j-3}+f_{j+3}) + \tfrac{107}{103,680}(f_{j-4}+f_{j+4})\end{aligned} \tag{5}$$

with modified stencil at the boundaries and periodicity in z-direction. The transfer function associated with this filter closely matches a Gaussian. The value $r=2$ is used in the present simulations, $\varepsilon_d = 0.025$ is set for the model coefficient.

RESULTS AND DISCUSSION

As it was hypothesized in experiments [10], confirmed in RANS simulations [8, 25] and further investigated in [21], rather complex flowfield with high levels of turbulence is created within the film cooling hole for the present cooling configuration. The effect of plenum-pipe interaction can be visualized by looking at instantaneous vorticity field. Instantaneous transverse vorticity $\omega_z d/U_\infty$ in $x-y$ centerplane is plotted in figure 3 for the pipe and the crossflow. At the downstream corner of the plenum-pipe connection, the flow undergoes a sharp 135 degree turning, carrying the large negative vorticity into the pipe. This is consistent with the clockwise rotation of the fluid particles bending around this corner. One can identify the trajectory of the fluid after it turns around the downstream plenum corner by the clearly marked strip of the negative vorticity inside the pipe. Not being able to make the sharp turn, the flow separates from the downstream wall and is carried towards the middle of the pipe. This separated fluid is brought back towards the downstream wall by the circular motion in the planes perpendicular to the pipe axis, which is documented in [21] with the help of instantaneous streamlines. Both positive and negative vorticity exists in this recirculation zone, marking the region of high-turbulence produced by the flow separation. The boundary layer on the upstream side of the wall identified by the strip of positive vorticity is relatively undisturbed and persists till the jet meets with the crossflow. It then bends into the crossflow direction and breaks into the rolling vortices with positive transverse vorticity marking the upper shear layer between the jet and the crossflow, where it interacts with the negative crossflow boundary layer vorticity. Region of high both positive and negative vorticity marking the zone with the high level of turbulence is observed in the region right behind the jet and in the jet wake above the wall.

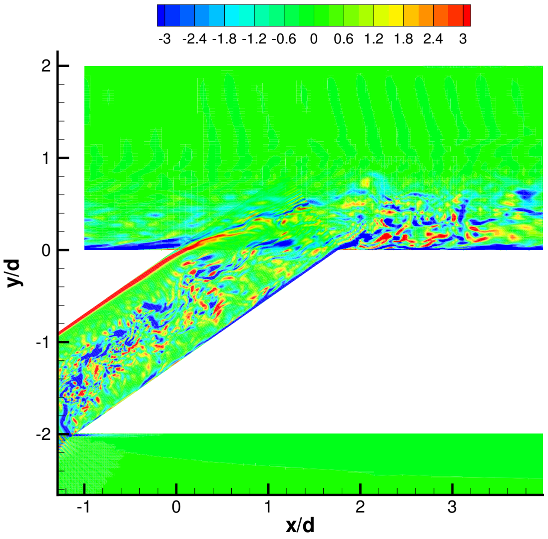

Figure 3. INSTANTANEOUS TRANSVERSE VORTICITY, $\omega_z d/U_\infty$, in $x-y$ CENTERPLANE FOR THE PIPE AND CROSSFLOW.

Instantaneous flowfield is highly irregular and the small-scale turbulent structures dominate the quasi-steady coherent vortices, when both the jet and the approaching crossflow are initially turbulent. Therefore, it is more instructive to look at the time-averaged quantities to investigate the flow dynamics. Time-averaged streamlines in the $x-y$ centerplane are shown in figure 4. The contours of the magnitude of time-averaged velocity $\sqrt{\tilde{u}^2+\tilde{v}^2+\tilde{w}^2}$ are also plotted, where $\tilde{}$ denotes Favre-averaged quantities. The zone of the reversed flow is observed right after the jet injection. It is marked by the node point in the streamline pattern in the $x-y$ centerplane. This node point coincides with the minimum of the mean velocity magnitude, as seen in figure 4. The region of reversed flow is also noticeable at the instantaneous streamlines pattern, see [21]. The fact that it persists in the time-averaged flowfield indicates that it is a steady structure of the flow. It is formed by the fluid wrapping around the jet and being tacked into its wake by the region of low pressure behind the jet. It is the common feature of jet-in-crossflow and is documented by many researchers.

We plot the magnitude of the mean velocity at the centerplane along the horizontal lines $y/d=0$ and $y/d=0.04$ in fig-

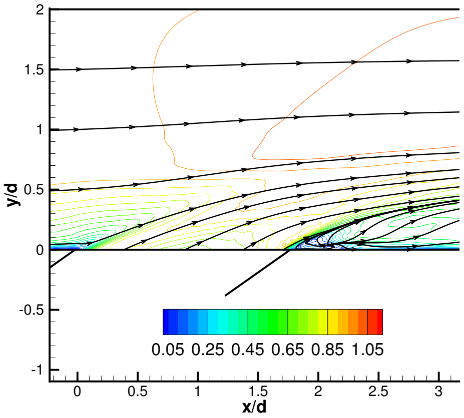

Figure 4. TIME-AVERAGED STREAMLINES SUPERIMPOSED ON THE CONTOURS OF THE MEAN VELOCITY MAGNITUDE $\sqrt{\tilde{u}^2+\tilde{v}^2+\tilde{w}^2}$, $x-y$ CENTERPLANE.

ure 5. The $y/d = 0.04$ line passes through the node point in the streamline pattern marking the center of the reversed flow zone. The region of minimum velocity right after the jet injection corresponding to the recirculating flow is seen for $y/d = 0.04$ plot. Looking at $y/d = 0$ plot, one can see that the jet exit velocity profile is non-uniform, with two distinct peaks - one on either side of the hole centerline. The leading peak is probably due to the separation inside the pipe, which mitigates the migration of the higher-momentum jet fluid towards the upstream wall. The trailing peak is most likely caused by the negative streamwise pressure gradient at the jet exit plane due to the crossflow blockage, forcing the jet to squeeze out of the downstream corner. The gap in the velocity magnitude in the center of the jet cross-section and its increase towards the periphery can also be identified by looking at the top view of the cross-section shown in figure 6. It is qualitatively similar to the plot of [2] for the velocity ratio $VR = 0.5$, however with some quantitative differences due to a higher velocity ratio of $VR = 0.64$ in the present study. It is worth noting that the contours of the instantaneous velocity in [21] look slightly different than that of the time-averaged. As it was already mentioned, the instantaneous flowfield is highly fluctuating and can not reflect the trends of the instantaneous flow.

Perhaps, the most attention from the researchers studying dynamics of jets in a crossflow has been on the counter-rotating vortex pair (CRVP), which is an inherent feature of jet-crossflow interaction. To determine an existence of CRVP in the present case, where inclined jets are issued from the short holes fed by a large sink-type delivery plenum, we look at the time-averaged streamlines superimposed on the contours of the normalized mean pressure in figure 7. Three streamwise cross-sections are shown: $x/d = 2.075$, $x/d = 3.55$ and $x/d = 5$, $x/d = 2.075$

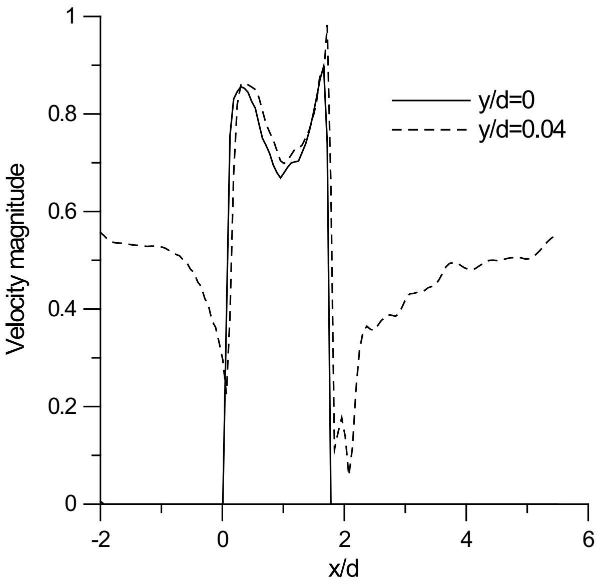

Figure 5. MAGNITUDE OF THE MEAN VELOCITY ALONG THE HORIZONTAL LINES $y/d = 0$ and $y/d = 0.04$, $x-y$ CENTERPLANE.

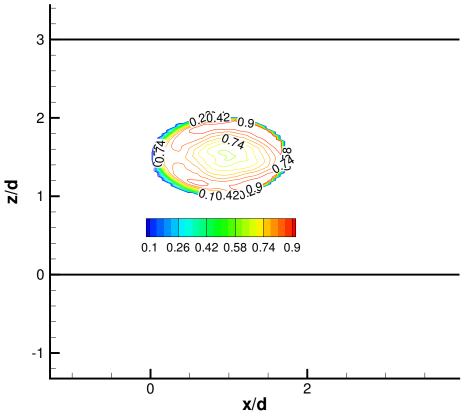

Figure 6. VELOCITY MAGNITUDE CONTOURS IN THE JET EXIT PLANE. THE TOP VIEW OF THE JET CROSS-SECTION.

passing through the node point in the streamline pattern of figure 4. The centers of CRVP generally coincide with the location of the pressure minimum, supporting the hypothesis of Muppidi et al. [26] that the mechanism responsible for the formation of CRVP is the global deformation of the jet cross-section driven by the pressure forces, rather than the reorientation of vorticity. The reorientation of either in-hole or jet shear layer vorticity definitely contributes to the strength of CRVP, but not causes its formation. The CRVP moves away from the wall as it convects

	DR	VR	BL	I
Sinha, ●	1.2	0.42	0.5	0.208
Sinha, △	1.2	0.5	0.6	0.3
LES	0.95	0.5	0.475	0.2375

Table 2. REGIME PARAMETERS FOR LES AND MEASUREMENTS OF SINHA ET AL.

downstream, in line with the vertical growth of the jet wake.

The documented features of the jet-crossflow interaction, such as reverse flow zone behind the jet and CRVP effect the distribution of the surface temperature. The crossflow fluid being involved in this recirculated motion is tucked beneath the jet and causes the wall temperature to increase. Strong CRVP vortices lift the cold jet away from the wall, decreasing the film cooling effectiveness. Film cooling effectiveness is defined as $\eta = (T_w - T_\infty)/(T_j - T_\infty)$, where T_w is the adiabatic wall temperature and T_j and T_∞ are the temperatures of the jet and a crossflow, respectively. To perform comparison with the cooling effectiveness measurements of Sinha et al. [27], we performed additional LES run with $VR = 0.5$ (as opposed to $VR = 0.64$ used to document the flowfield in the above discussion), to match the $VR = 0.5$ case of [27]. The comparison is shown in figure 8. Although we do match the velocity ratio for the experimental data shown with triangles, there are other important parameters describing the film cooling process, like density ratio DR, blowing ratio $BL = \rho_j U_j / \rho_\infty U_\infty$ and momentum ratio $I = \rho_j U_j^2 / \rho_\infty U_\infty^2$. The value of these four parameters for our LES and for measurements of Sinha et al. indicated by bullets and triangles are summarized in table 2. It is shown in [27] that the film cooling effectiveness data is best collapsed with the momentum ratio. The simulated momentum ratio lies between the two experimental values. Present simulations document the region of sharp decrease in effectiveness due to the jet lift off observed in Sinha, △, but the cooling effectiveness recovers to the higher value, matching more the value of the Sinha, ●, and the recovery seems to happen faster. It might be due to the fact that the reverse flow zone, although exists, spreads less distance in streamwise direction for the current regime. It is worth mentioning the main advantage of LES versus RANS techniques when applied to film cooling flows in the context of the film cooling effectiveness. The main problem of RANS is the inability to resolve the reverse flow zone behind the jet and the jet lift off, resulting in higher centerline effectiveness than the documented experimental values for all the regimes (see [2, 8]). The current LES is definitely capable of resolving this zone and does not overpedict the centerline effectiveness.

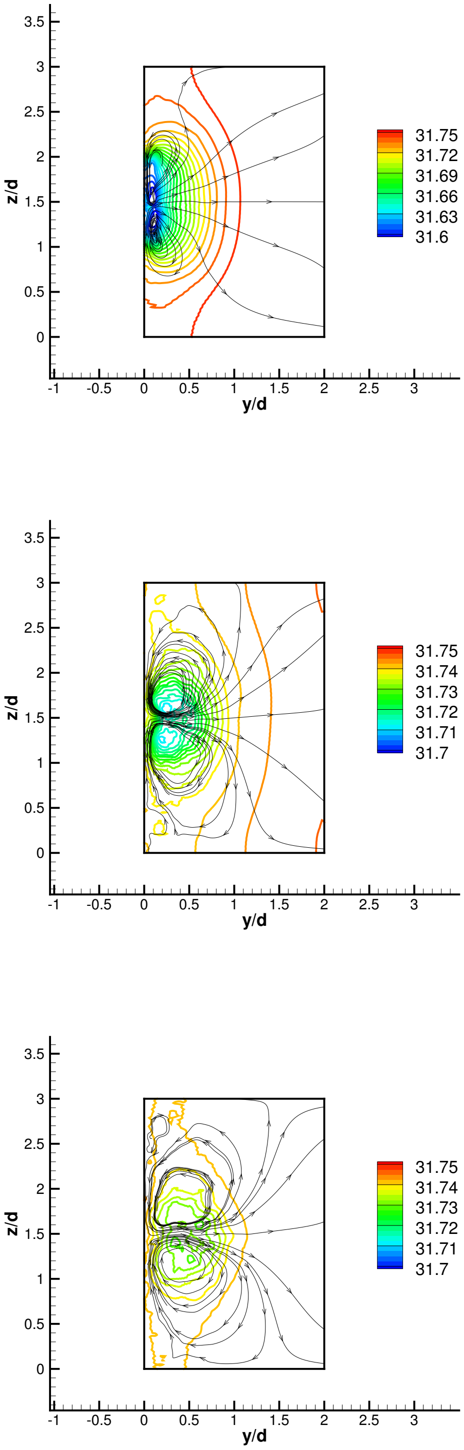

Figure 7. TIME-AVERAGED STREAMLINES SUPERIMPOSED ON THE CONTOURS OF NORMALIZED MEAN PRESSURE. TOP FIGURE: $x/d = 2.075$, MIDDLE: $x/d = 3.55$, BOTTOM: $x/d = 5$

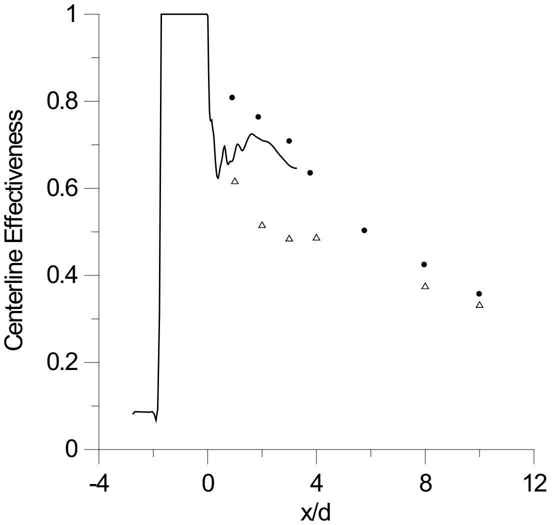

Figure 8. CENTERLINE FILM COOLING EFFECTIVENESS. ——, current LES; ●, Sinha et al. $VR = 0.42$; △, Sinha et al. $VR = 0.5$;

CONCLUSIONS

The experimental set-up of Pietrzyk et al. [10] is modeled numerically, using Large Eddy Simulation technique. Time-averaged flowfield is analyzed in order to identify quasi-steady coherent structures of the flow. Among these structures are: the separated flow inside the film hole, reverse flow zone right after the jet injection and counter-rotating vortex pair. These structures are important in understanding film cooling physics, since they effect the distribution of the surface temperature, and, as a result, the cooling performance parameters, such as film cooling effectiveness. Comparison of the computed centerline effectiveness with the experimental data shows favorable agreement and confirms the superiority of LES versus RANS in predicting the thermal field of film cooling flows.

ACKNOWLEDGMENT

This work is supported by the Advanced Simulation and Computing (ASC) program of the Department of Energy. The compressible code was developed with AFOSR support under grant No. F94620-01-1-0138. Computer time is provided by ARL and ERDC High-Performance Supercomputer Centers at the Department of Defense. We would like to thank Dr. Bogard for providing the experimental database for comparison.

REFERENCES

[1] Burd, S. W., Kaszeta, R. W., and Simon, T. W., 1998. "Measurements in film cooling flows: Hole l/d and turbulence intensity effects". *Transactions of the ASME. The Journal of Turbomachinery,* **120**, Oct., pp. 791–798.

[2] Walters, D. K., and Leylek, J. H., 2000. "A detailed analysis of film-cooling physics: Part i - streamwise injection with cylindrical holes". *Transactions of the ASME. The Journal of Turbomachinery,* **122**, Jan., pp. 102–112.

[3] Hyams, D. G., and Leylek, J. H., 2000. "A detailed analysis of film-cooling physics: Part iii - streamwise injection with shaped holes". *Transactions of the ASME. The Journal of Turbomachinery,* **122**, Jan., pp. 122–132.

[4] Peterson, S. D., and Plesniak, M. W., 2004. "Evolution of jets emanating from short holes into crossflow". *Journal of Fluid Mechanics,* **503**, pp. 57–91.

[5] Bohn, D., Becker, V., and Kusterer, K., 2000. "Three-dimensional flow analysis of turbine balde cascades with leading-edge ejection". *Journal of Propulsion and Power,* **16**(1), Jan., pp. 49–56.

[6] Tyagi, M., and Acharya, S., 2003. "Large eddy simulation of film cooling flow from an inclined cylindrical jet". *Transactions of the ASME. The Journal of Turbomachinery,* **125**(4), Oct., pp. 734–742.

[7] Liu, K., and Pletcher, R., 2005. Large eddy simulation of discrete-hole film cooling in a flat plate turbulent boundary layer. AIAA Paper 2005–4944, June. In 35th AIAA Fluid Dynamics Conference and Exhibit.

[8] Leylek, J. H., and Zerkle, R., 1994. "Discrete-jet film cooling: A comparison of computational results with experiments". *Transactions of the ASME. The Journal of Turbomachinery,* **116**, July, pp. 358–368.

[9] Medic, G., and Durbin, P. A., 2002. "Toward improved film cooling prediction". *Transactions of the ASME. The Journal of Turbomachinery,* **124**, Apr., pp. 193–199.

[10] Pietrzyk, J. R., Bogard, D. G., and Crawford, M. E., 1989. "Hydrodynamic measurements of jets in crossflow for gas turbine film cooling applications". *Transactions of the ASME. The Journal of Turbomachinery,* **111**, Apr., pp. 139–145.

[11] Xiong, Z., and Lele, S. K., 2001. Numerical study of leading edge heat transfer under free-stream turbulence. AIAA Paper 2001–1016, Jan. In 39th AIAA Aerospace Sciences Meeting and Exhibit.

[12] Xiong, Z., 2004. Stagnation point flow and heat transfer under free-stream turbulence. Ph.d. thesis, Aug. Deparment of Mechanical Engineering, Stanford University.

[13] Pierce, C. D., 2001. Progress-variable approach for large eddy simulaiton of turbulent combustion. Ph.d. thesis, June. Deparment of Mechanical Engineering, Stanford University.

[14] Harlow, F. H., and Welch, J. E., 1965. "Numerical calculation of time-dependent viscous incompressible flow". *Physics of Fluids,* **8**, pp. 2182–2189.

[15] Leonard, B. P., 1979. "A stable and accurate convective modelling procedure based on quadratic upstream interpolation". *Computational Methods in Applied Mechanics and*

Engineering, **19**, pp. 59–98.

[16] Germano, M., Piomelli, U., Moin, P., and Cabot, W. H., 1991. “A dynamic subgrid-scale eddy viscosity model”. *Physics of Fluids, A3*, pp. 1760–1765.

[17] Iourokina, I. V., and Lele, S. K., 2005. Towards largy eddy simulation of film-cooling flows on a model turbine blade leading edge. AIAA Paper 2005–0670, Jan. In 43rd AIAA Aerospace Sciences Meeting and Exhibit.

[18] Müller, B., 1999. “Low Mach number asymptotics of the navier-stokes equations and numerical implicatons”. In 30th Computational Fluid Dynamics, von Karman Institute for Fluid Dynamics, Lecture Series 1999–03, pp. 821–831.

[19] Lund, T. S., Wu, X., and Squires, K. D., 1998. “Generation of turbulent inflow data for spatially-developing bounday layer simulations”. *Journal of Computational Physics,* **140**, pp. 233–258.

[20] Xu, S., and Martin, M. P., 2004. “Asesment of inflow boundary conditions for compressible turbulent boundary layers”. *Physics of Fluids,* **16**(7), July, pp. 2623–2639.

[21] Iourokina, I. V., and Lele, S. K., 2006. Largy eddy simulation of film-cooling above the flat surface with a large plenum and short exit holes. AIAA Paper 2006–1102, Jan. In 44th AIAA Aerospace Sciences Meeting and Exhibit.

[22] Cook, A. W., and Cabot, W. H., 2004. “A high-wavenumber viscosity for high-resolution numerical methods”. *Journal of Computational Physics,* **195**, pp. 594–601.

[23] Cook, A. W., and Cabot, W. H., 2005. “Hyperviscosity for shock-trubulent interactions”. *Journal of Computational Physics,* **203**, pp. 379–385.

[24] Fiorina, B., and Lele, S. K., 2005. “An artificial nonlinear diffusivity method for supersonic reacting flows with shocks”. *Journal of Computational Physics, Submitted for publication*.

[25] Walters, D. K., and Leylek, J. H., 1997. “A systematic computational methodology applied to a three-dimensional film-cooling flowfield”. *Transactions of the ASME. The Journal of Turbomachinery,* **119**, Oct., pp. 777–785.

[26] Muppidi, S., and Mahesh, K., 2006. Passive scalar mixing in jets in crossflow. AIAA Paper 2006–1098, Jan. In 44th AIAA Aerospace Sciences Meeting and Exhibit.

[27] Sinha, A. K., Bogard, D. G., and Crawford, M. E., 1991. “Film-cooling effectiveness downstream of a single row of holes with variable density ratio”. *Transactions of the ASME. The Journal of Turbomachinery,* **113**, July, pp. 442–449.